Proposal for a Spin-Torque-Oscillator Maser Enabled by Microwave Photon-Spin Coupling

Justin T. Hou, Pengxiang Zhang, and Luqiao Liu[*]

Department of Electrical Engineering and Computer Science, Massachusetts Institute of Technology, Cambridge, Massachusetts 02139, USA

We study a direct-current-driven maser device enabled by spin-photon coupling, where coherent magnetic self-oscillation can be realized in a large-area ferromagnetic thin film under the excitation of spin-orbit torques. We show via both micromagnetic simulation and analytical derivation that above a critical value of the coupling strength between the spin-torque oscillator and the microwave resonator, magnetic oscillation develops macroscopic phase coherence, a narrow linewidth, and becomes phase-locked with the photon mode. The threshold coupling strength for synchronizing individual spins reduces as the sample dimension increases, suggesting that the spin-torque-oscillator maser can be readily realized using large-area thin-film ferromagnets without relying on dimension confinement. Moreover, the photon mode can directly provide microwave emission, which exhibits enhanced power and a reduced linewidth with an increasing number of spins, leading to a useful approach for developing highly coherent on-chip microwave sources.

I. INTRODUCTION

Spin-torque oscillators (STOs) [1,2] have been extensively studied for realizing on-chip microwave sources [3–5], detectors [6], and components for neuromorphic applications [7,8]. STOs have first been realized with the spin-transfer torque effect in quasi-zero-dimensional magnetic systems, such as magnetic tunnel junctions [9], nanopillar spin valves [3,10,11], and nanocontacts [4]. Nanoscale quasi-single-domain structures are generally required in these experiments, since the needed excitation current scales quickly with the magnetic area. The discovery of the spin-orbit torque effect opened up the possibility of exciting magnetic oscillations on a larger area, as a charge current flowing across a very small cross section can now inject spins into a magnetic film with a much larger area [12–15]. However, coherent magnetic self-oscillation over an extended ferromagnetic thin film has proven to be hard due to the existence of a continuous magnon band, under which magnon excitations are quickly scattered into different modes, losing the global phase coherence [16,17]. To restrain this decoherence process, dimension confinement has been introduced to discretize magnon bands and to enforce coherent oscillation of spins at different regions of the oscillator [15,18]. Under the size limit imposed by the coherence requirement, various methods have been utilized to overcome the power bottleneck from a single nanoscale STO, including synchronizing different STOs

through electrical connections [19,20], spin wave interactions [21–24], and dipolar interactions [25,26], which introduce complexities in circuit design and device fabrication. On the other hand, the small volume of STOs renders them susceptible to thermal fluctuations [1,27]. Therefore, different approaches have been pursued to achieve linewidth reduction with the aid of external circuits and signals [28–32].

In this paper, we propose an approach for realizing magnetic self-oscillation in a large-area ferromagnetic thin film with high emission power and narrow linewidth, by exploiting spin-photon coupling. Hybrid magnon-photon systems have recently attracted great attention for reaching coherent information processing and transduction [33–40]. On-chip architecture with a large magnon-photon coupling strength has been demonstrated for potentially scalable device applications [41,42]. The integration of an active spintronic device with the photon mode in a microwave cavity is therefore highly attractive for bringing new functions to these hybrid systems. Here, with micromagnetic simulations and analytical derivation, we study the magnetic dynamics of an STO located within a microwave cavity, driven by antidamping spin-orbit torque from a direct current (dc). We find that under a strong enough coupling between an STO and a cavity, spontaneous magnetic oscillations with macroscopic phase coherence can be achieved without any externally applied locking signals, even in large-size ferromagnetic thin films. Moreover, with the increase of the number of spins in the magnetic film N_s, the coupling strength needed for overcoming the

*luqiao@mit.edu

synchronization threshold decreases, the microwave output power increases, and the oscillation linewidth becomes narrower. The idea of using a cavity to realize highly coherent emission is rooted in the design principles of the laser or maser [43–45], where the phase coherence in different regions of the nonlinear gain medium is enforced by a global coupling mechanism—cavity photons—rather than short-range forces such as dipolar or exchange interactions in conventional STOs.

II. RESULTS

A. Micromagnetic equations

Figure 1(a) shows a schematic of our proposed device. A spin-current density J_s for generating dampinglike torque is injected into a ferromagnetic thin film, the dynamics of which are coupled with the cavity photon mode. This microwave cavity can be experimentally realized with the usage of on-chip two-dimensional resonators for the small mode volume and the high spin-photon coupling strength [41,42]. The system can be represented as the circuit diagram shown in Fig. 1(b). We assume that the frequencies of the higher-order modes of the resonator are far away from its fundamental mode and that the dimension of the ferromagnetic device is small compared with the wavelength of this fundamental mode. Therefore, for the spectrum region of interest, the microwave resonator can be modeled as a serial LCR circuit. In the presence of a resonator current, each spin experiences an oscillating magnetic field $\mathbf{B_{rf}}$ generated by the inductor. For an on-chip resonator design, $\mathbf{B_{rf}}$ is uniformly polarized across the magnetic device in one specific direction. For the configuration shown in Fig. 1(b), to induce maximal spin-photon coupling, we set $\mathbf{B_{rf}} = b_{rf} I \hat{\mathbf{x}}$ along the x direction, which is perpendicular to external biasing field $\mathbf{B}_0 = B_0 \hat{\mathbf{y}}$. Here, b_{rf} is the rf field generated per unit inductor current I. For the circuit

shown in Fig. 1(b), $\mathbf{B_{rf}}$ generated by the inductor loop at the magnet location $\vec{r}'$ can be written as $\mathbf{B_{rf}}(\vec{r}') = \mathbf{b_{rf}}(\vec{r}')I$, where $\mathbf{b_{rf}}(\vec{r}') = \oint_L (\mu_0/4\pi)[(\vec{r}-\vec{r}') \times \hat{i}_l(\vec{r})/|\vec{r}-\vec{r}'|^3]dl = b_{rf}\hat{\mathbf{x}}$, with the integral taken along $\vec{r}$ on the inductor loop. Here, $\hat{i}_l(\vec{r})$ is the unit vector along the current flowing direction in the inductor. The dynamics of the hybrid system can be modeled as follows:

$$\frac{d\hat{\mathbf{m}}_i}{dt} = \boldsymbol{\tau}_i - \gamma \hat{\mathbf{m}}_i \times \mathbf{b_{rf}}I, \tag{1}$$

$$\frac{dI}{dt} = \frac{V}{L} - \frac{R}{L}I - \frac{b_{rf}M_sV_c}{L}\sum_i \frac{d\hat{m}_{xi}}{dt} + f_I(t), \tag{2}$$

$$\frac{dV}{dt} = -\frac{I}{C} + f_V(t). \tag{3}$$

Here, we employ a micromagnetic approach by considering a magnetic free layer in an STO consisting of N_c cells. γ is the gyromagnetic ratio. $\hat{\mathbf{m}}_i$ is the unit vector representing the magnetic moment direction of cell i. $\boldsymbol{\tau}_i$ is the total torque acting on $\hat{\mathbf{m}}_i$ considered in standard micromagnetic simulations, including contributions from the Zeeman field, the anisotropy field, the exchange field, and the dipolar field, as well as from Gilbert damping and spin torque [46]. The second torque term on the right-hand side of Eq. (1) originates from the Oersted field from the LCR resonator. On the other hand, because of Faraday's law, the oscillating magnetic moment leads to an electromotive force onto the inductor, which is proportional to the time change of the magnetic flux λ through the inductor loop: $\lambda = \sum_i \oint_L \vec{A}_i(\vec{r}) \cdot \hat{i}_l(\vec{r})dl$, where $\vec{A}_i(\vec{r}) = (\mu_0/4\pi)[M_sV_c\hat{\mathbf{m}}_i \times (\vec{r}-\vec{r}')/|\vec{r}-\vec{r}'|^3]$ is the vector potential at position $\vec{r}$ generated by the magnetic moment $M_sV_c\hat{\mathbf{m}}_i$ of cell i at location $\vec{r}'$, with V_c being the cell volume and M_s being the saturation magnetization. Using the previous expression of $\mathbf{b_{rf}}(\vec{r}')$, we can rewrite $\lambda = M_sV_c \sum_i \hat{\mathbf{m}}_i \cdot \mathbf{b_{rf}}(\vec{r}')$. Therefore, the electromotive force is

(a) **(b)**
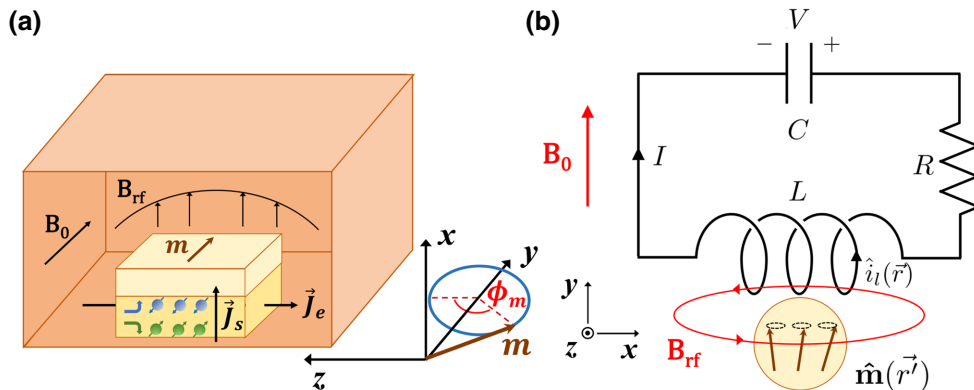
FIG. 1. (a) A schematic of the considered device structure. A magnetic oscillator driven by spin-orbit torque is placed inside a microwave cavity and inductively coupled to the cavity photon mode. (b) The effective circuit diagram. The microwave cavity is modeled as a serial LCR circuit. The magnetic thin film is coupled with the LCR circuit through the rf magnetic field $\mathbf{B_{rf}}$ generated by the inductor current. No external signals are used to drive the LCR circuit.

given by $-b_{rf}M_sV_c\sum_i(d\hat{m}_{xi}/dt)$ in Eq. (2), with $\hat{m}_{xi}$ being the projection of the $\hat{\mathbf{m}}_i$ vector along the x direction. Equations (2) and (3) therefore describe the dynamics of the current I and voltage V of the LCR resonator in the presence of magnetic oscillations. The only external drive of the whole system is the dc spin torque included in τ_i. To account for the thermal fluctuation at finite temperature T, we include the torque from the thermal magnetic field in the dynamics of $\hat{\mathbf{m}}_i$ in Eq. (1) [46], as well as white Gaussian thermal noise $f_I(t)$ and $f_V(t)$ in Eqs. (2) and (3). The latter two noise terms satisfy the fluctuation-dissipation relation of the LCR circuit, with $\langle f_I(t)f_I(t')\rangle = Rk_BT/L^2\delta(t - t')$ and $\langle f_V(t)f_V(t')\rangle = Rk_BT/LC\delta(t - t')$, respectively [1, 27] (for a derivation, see Appendix A). Here, k_B is the Boltzmann constant. To numerically solve the $N_c + 2$ coupled dynamical equations, we augment the ordinary differential equation solver for Landau-Lifshitz-Gilbert (LLG) equations with an additional torque term in Eq. (1) and introduce new time-dependent quantities I and V by modifying the micromagnetic package MUMAX3 [46]. f_I and f_V are implemented according to $f_I(t_n) = \eta_I(t_n)\sqrt{Rk_BT/(L^2\Delta t)}$ and $f_V(t_n) = \eta_V(t_n)\sqrt{Rk_BT/(LC\Delta t)}$, where $\eta_I(t_n)$ and $\eta_V(t_n)$ are random numbers from the standard normal distribution, the values of which are changed after every time step with step size $\Delta t = t_n - t_{n-1}$ [46]. Our modified simulation codes are available online [47].

B. Micromagnetic simulation results

We compare the magnetic dynamics of an STO with and without being coupled onto a microwave resonator. For micromagnetic simulation, we set the ferromagnetic film to be a circular disk with diameter D for simplicity. We verify that the observations in the following apply to other geometries such as rectangles or long wires. The film thickness is 5 nm and each magnetic cell is a cuboid with size 2.5 nm × 2.5 nm × 5 nm. We set the saturation magnetization $M_s = 5.5 \times 10^5 A/m$, the exchange stiffness $A_{ex} = 9$ pJ/m, and the Gilbert damping coefficient $\alpha = 0.04$. To reduce the threshold current and minimize nonlinear damping [48], we introduce a perpendicular anisotropy field of $B_a = 0.66$ T to partially cancel the demagnetization field. The ferromagnet is biased with a dc field along the y axis, $B_0 = 0.18$ T, and a dc spin current $J_s = 1.0 \times 10^{11}$ A/m^2, which is larger than the oscillation threshold current for all of the cases considered below. Except for the spin current, no external dc or ac drives are assumed on the STO-resonator system. The parameters of the serial LCR resonator are chosen as $L = 1.56$ nH, $C = 0.637$ pF, and $R = 0.05$ Ω, which lead to characteristic impedance $Z = \sqrt{L/C} = 50$ Ω, a quality factor of $Q = Z/R = 1000$, and the resonant frequency $\omega_r = 1/\sqrt{LC} = 2\pi \times 5$ GHz, close to the uniform ferromagnetic resonance (FMR) frequency $\omega_0 = \gamma\sqrt{B_0(B_0 + \mu_0 M_{eff})} \approx 2\pi \times 5.44$ GHz of the ferromagnetic film. Figure 2(a) shows the
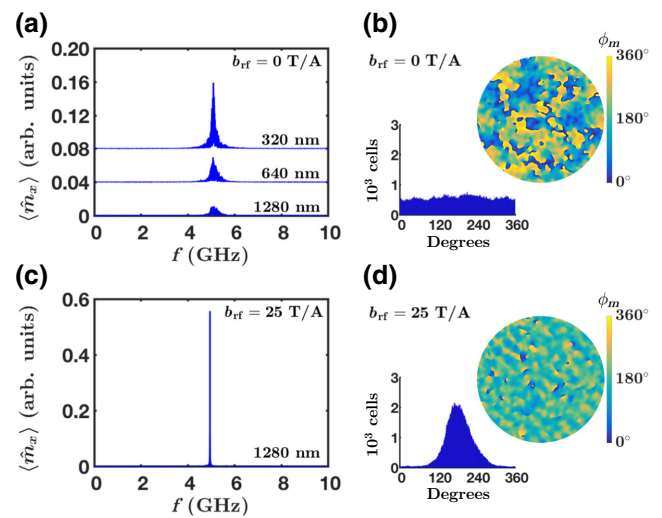
FIG. 2. Micromagnetic simulation results of STOs without [(a),(b)] and with [(c),(d)] coupling onto a microwave resonator. (a),(c) The Fourier transform of $\langle \hat{m}_x \rangle$. (b),(d) The real-space distribution of the magnetization azimuthal angle ϕ_m in the x-z plane with $D = 1280$ nm. The histograms in the insets show the number of cells as a function of ϕ_m, with the bins chosen to be 1°. T is set to be 0 K in the simulations of this figure.

simulation results in the absence of an LCR resonator ($b_{rf} = 0$ T/A), where the Fourier transform of the x component of the magnetic oscillation $\langle \hat{m}_x \rangle$ is illustrated for $D = 320, 640,$ and 1280 nm at $T = 0$ K. With the increase of the device size, the current-induced magnetic oscillation loses coherence, where the peak power decreases and the linewidth increases, consistent with previous experimental observations [16,17]. An inspection on the real-space distribution of the magnetization azimuthal angle ϕ_m [see Fig. 1(a) for a definition] shows that the lack of phase coherence of magnetic dynamics in different cells accounts for the small signal and the broad linewidth [Fig. 2(b)]. The simulation results with finite spin-photon coupling ($b_{rf} = 25$ T/A) are shown in Fig. 2(c) for the $D = 1280$ nm sample. In contrast to the uncoupled case, $\langle \hat{m}_x \rangle$ exhibits a much larger oscillation amplitude and a much narrower linewidth. Moreover, the real-space distribution of ϕ_m shows that inhomogeneities are greatly suppressed, indicating the realization of macroscopically coherent magnetic self-oscillation [Fig. 2(d)].

To understand the required condition for reaching coherent magnetic oscillations, we carry out simulations for the $D = 1280$ nm sample under different external fields B_0. As shown in Fig. 3(a), when the detuning between the STO free-running frequency ω_S and the resonator frequency ω_r is small ($0.176T < B_0 < 0.208T$), ω_S is locked onto ω_r. We further verify that within the frequency-locking region, the relative phase difference between the resonator and the STO remains nearly constant as a function of time, indicating phase locking. Next, we fix $B_0 = 0.18$ T and study

the STO dynamics as a function of the coupling coefficient b_{rf} [Fig. 3(b)]. We note that below a critical value $b_{rf,c}$, the oscillation amplitude on the x-z plane $\langle \hat{m}_{xz} \rangle$ remains almost zero, while above $b_{rf,c}$ it jumps to a much higher value, indicating a transition from incoherent to coherent oscillation. In Fig. 3(c), we plot the dependence of $b_{rf,c}$ on the spin number N_s by carrying out simulations on samples with different sizes. We find that the threshold coupling coefficient decreases as N_s increases, satisfying a relationship of $b_{rf,c} \propto 1/\sqrt{N_s}$, a result that can be further verified through analytical derivation (see Sec. C). The scaling relation of $b_{rf,c} \propto 1/\sqrt{N_s}$ implies that it is easier to achieve coherent oscillations in samples with large N_s, e.g., with an extended thin film. b_{rf} is a factor that depends on the *LCR* resonator geometry and the proximity of the magnetic material to the inductor. For a two-dimensional on-chip resonator design with a simple inductive wire [42], one has the relation of $b_{rf} = \mu_0/2w$, where w is the inductive wire width. Previously, it has been shown that with lithographically defined superconducting resonators, b_{rf} on the order of 0.1 T/A can be achieved [42]. By extrapolating the results in Fig. 3(c), we see that with this b_{rf}, synchronized oscillations can be reached in samples with $N_s > 10^{13}$, corresponding to a lateral dimension of approximately 200 μm. Besides allowing easier synchronization with the resonator mode, a larger magnetic volume is also beneficial for increasing the emission power. In Fig. 3(d), we study the energy stored in the resonator E_r as a function of the sample size, which shows a linear increase with N_s, providing a promising approach to overcoming the power bottleneck encountered in classical STOs. Moreover, different from previous STO designs where the magnetic oscillation needs to be converted to an output signal through certain magnetoresistance effects [2], the resonator can directly provide microwave emission to the external circuit, the strength of which depends on the stored energy as well as the coupling with the external circuit [49].

C. Analytical theory for oscillator synchronization

The cavity-assisted coherent magnetic self-oscillation can be further verified and extended with analytical studies. We rewrite Eqs. (1)–(3) in complex oscillator representation, following Slavin *et al.* [1,50] (see Appendices B and C):

$$\frac{dc_i}{dt} + i\omega_i(p_i)c_i + \Gamma_i(p_i)c_i = F_{mi}(c_r) + \sum_{i \neq j} G_{ji}(c_i, c_j),$$

$$(4)$$

$$\frac{dc_r}{dt} + i\omega_r c_r + \frac{\omega_r}{2Q}c_r = \sum_i F_{ri}(c_i).$$

$$(5)$$

Here, c_i, defined as a superposition of $\hat{m}_{xi}$ and $\hat{m}_{zi}$ by taking into account the elliptical oscillation orbit [1,50], is the
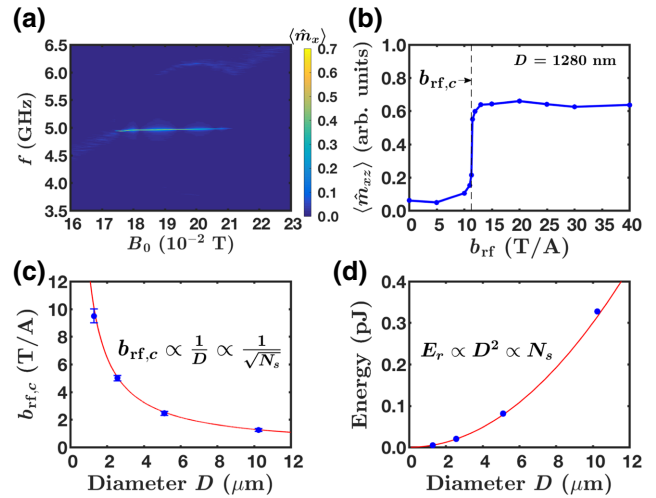
FIG. 3. (a) The Fourier transform of $\langle \hat{m}_x \rangle$ as a function of B_0. In this simulation, $b_{rf} = 25$ T/A and $D = 1280$ nm. (b) The average magnetization projected onto the x-z plane, $\langle \hat{m}_{xz} \rangle$, as a function of the spin-photon coupling coefficient b_{rf}. The incoherence-to-coherence transition happens at $b_{rf,c} \approx 11.3$ T/A. (c) $b_{rf,c}$ as a function of the ferromagnetic disk diameter D. The red curve shows the result from analytical modeling. N_s is the number of spins in the disks. (d) The energy stored in the resonator E_r as a function of diameter D. $b_{rf}D$ is kept constant in simulations with different sample sizes, with $b_{rf} = 15$ T/A for $D = 1280$ nm. The red curve represents the analytical results. The simulation cell size is 2.5 nm × 2.5 nm × 5 nm for (a) and (b) and 10 nm × 10 nm × 5 nm for (c) and (d). T is set to be 0 K in simulations of this figure. In (c) and (d), B_0 and J_s are fixed in simulations with different diameters.

dimensionless complex oscillation amplitude for magnetic cell i with power $p_i = |c_i|^2$ and phase $\phi_i = \arg(c_i)$. In our simulations with nearly compensated magnetic anisotropy, we have $c_i \approx (\hat{m}_{zi} - j\hat{m}_{xi})/\sqrt{2(1 + \hat{m}_{yi})}$, where $j = \sqrt{-1}$. $\omega_i(p_i)$ is the power-dependent self-oscillation frequency, which is related to the effective field experienced by each cell. Under a first-order approximation, $\omega_i(p_i) = \omega_{0i} + K_i p_i$, with $K_i = (d\omega_i/dp_i)$. $\Gamma_i(p_i) = \Gamma_{i,+}(p_i) - \Gamma_{i,-}(p_i)$ is the nonlinear damping coefficient, which includes both positive Gilbert damping $\Gamma_{i,+}(p_i)$ and negative effective damping $\Gamma_{i,-}(p_i)$ from spin torque. $c_r = I + iV/Z = \sqrt{p_r}e^{i\phi_r}$ is the complex amplitude of the *LCR* resonator with intrinsic frequency ω_r and dissipation rate $\omega_r/2Q$. $F_{ri}(c_i) = -g_{ri}c_i$ and $F_{mi}(c_r) = g_m c_r$ reflect the mutual coupling between the ith magnetic cell and the *LCR* resonator, with $g_{ri} = \omega_{0i}b_{rf}M_sV_c/L$ and $g_m = \gamma b_{rf}/4$ in the case of nearly compensated magnetic anisotropy. Meanwhile, the magnetic cells are also coupled with each other through G_{ji}, which includes exchange and dynamic dipolar interactions between cell i and cell j. Without G_{ji} and F_{mi}, the magnetization in each cell i self-oscillates independently at frequency $\omega_{gi} = \omega_i(p_{i0})$, with the equilibrium power p_{i0} satisfying $\Gamma_i(p_{i0}) = 0$, and no global coherence

is expected. The existence of short-range interaction G_{ji}, on the other hand, allows coherent oscillations from small quasi-single-domain samples, as shown in previous experiments [2]. However, it has been demonstrated that the short-range interactions become less efficient and that they cannot lead to global phase synchronization when the size of the sample goes to infinity [51,52]. For this reason and also to obtain a closed mathematical form, we only consider the interactions between the magnetic cells and the *LCR* resonator, F_{mi} and F_{ri}, in the following analytical derivation and rely on the full micromagnetic solution to check the extra influences resulting from the short-range interactions G_{ji}.

Isolating c_i into its phase and power parts, the coupled dynamics of the system are captured by the equations on the magnetic cell phase ϕ_i and the resonator amplitude c_r:

$$\frac{d\phi_i}{dt} + \omega_{gi} = g_m\sqrt{1 + \nu_i^2}\sqrt{\frac{p_r}{p_{i0}}}\sin(\phi_r - \phi_i - \beta_i), \quad (6)$$

$$\frac{dc_r}{dt} + i\omega_r c_r + \frac{\omega_r}{2Q}c_r = \sum_i -g_{ri}\sqrt{p_{i0}}e^{i\phi_i}, \quad (7)$$

where $\nu_i = K_i/(G_{+,i} - G_{-,i})$ is a parameter quantifying the frequency nonlinearity of the STO [1], with $G_{+,i} = (d\Gamma_{+,i}/dp_i)|_{p_{i0}}$, $G_{-,i} = (d\Gamma_{-,i}/dp_i)|_{p_{i0}}$, and $\beta_i = \arctan(\nu_i)$. To capture the main physics of the coupled phase oscillators, we set all parameters except ω_{gi} to their average values $\nu_i = \nu$, $p_{i0} = p_0$, $\beta_i = \beta_m$, and $g_{ri} = g_r$. In the limit of large N_c, we assume that the frequency and phase distribution of magnetic cells satisfy a probability density function $f(\phi, \omega, t)$, where $f(\phi, \omega, t)d\phi d\omega$ describes the fraction of cells in phase $(\phi, \phi + d\phi)$ and frequency $(\omega, \omega + d\omega)$ [53]. To describe the coherence of the STO, we define the phase order parameter,

$$\Psi = \frac{1}{N_c}\sum_i e^{i\phi_i} = \int_{-\infty}^{\infty} d\omega \int_0^{2\pi} f(\phi, \omega, t)e^{i\phi}d\phi, \quad (8)$$

and we can rewrite Eqs. (6) and (7) as

$$\frac{d\phi}{dt} + \omega = g_m\sqrt{1 + \nu^2}\sqrt{\frac{p_r}{p_0}}\sin(\phi_r - \phi - \beta_m), \quad (9)$$

$$\frac{dc_r}{dt} + i\omega_r c_r + \frac{\omega_r}{2Q}c_r = -g_r\sqrt{p_0}N_c\Psi. \quad (10)$$

According to probability conservation, the probability function $f(\phi, \omega, t)$ satisfies a continuity equation:

$$\frac{\partial f}{\partial t} + \frac{\partial}{\partial \phi}\left(f\frac{d\phi}{dt}\right) = 0, \quad (11)$$

where $(d\phi/dt)$ is given by Eq. (9).

Equations (9)–(11) give a description on the time evolution of the phase distribution of the coupled magnetic cells.

To solve this equation set, we follow the Ott-Antonsen ansatz [53,54] and have a tentative solution $f(\phi, \omega, t)$ expressed in a Fourier series:

$$f(\phi, \omega, t) = \frac{h(\omega)}{2\pi}\left[1 + \sum_{n=1}^{\infty}[\alpha(\omega, t)]^n e^{in\phi} + c.c.\right], \quad (12)$$

where the Fourier coefficients take the functional form of $[\alpha(\omega, t)]^n$. This type of solution has been proven to be useful for describing systems with a large number of oscillators. In Eq. (12), $h(\omega) = \int_0^{2\pi} f(\phi, \omega, t)d\phi$ is the distribution of the generation frequency of magnetic cells. The coupled Eq. (9)–(11) are solvable when the form of the frequency distribution $h(\omega)$ is specified. Here, to obtain a closed-form analytical solution, we assume that the frequency distribution follows the Lorentzian distribution $h(\omega) = (\Delta_m/\pi)[(\omega - \bar{\omega})^2 + \Delta_m^2]^{-1}$, with a central frequency of $\bar{\omega}$ and linewidth Δ_m. Under this choice of frequency distribution, the phase order parameter has a simple expression $\Psi = [\alpha(\bar{\omega} + i\Delta_m, t)]^*$. Substituting Eqs. (12) and (9) into Eq. (11), we find that the order parameter obeys the following dynamical equation:

$$\frac{d\Psi}{dt} + i(\bar{\omega} - i\Delta_m)\Psi = \frac{g_m\sqrt{1 + \nu^2}}{2\sqrt{p_0}}\left[c_r e^{-i\beta_m} - \Psi^2 c_r^* e^{i\beta_m}\right], \quad (13)$$

which, together with Eq. (10), describes the dynamics of the system.

Equations (10) and (13) are two coupled differential equations with respect to Ψ and c_r. The bifurcation point of the dynamical system described by these two equations can be obtained via linear stability analysis. By assuming solutions of $\Psi = \Psi_0 e^{(\lambda - i\Omega)t}$ and $c_r = c_{r0}e^{(\lambda - i\Omega)t}$ and substituting them into Eqs. (10) and (13), we find that the nontrivial solution of $|\Psi| \neq 0$ becomes the stable one when the coupling coefficient b_{rf} exceeds a threshold value of $b_{rf,c}$, which has the following simple expression:

$$b_{rf,c} = \sqrt{\frac{4Z\Delta_m}{\gamma\omega_0 QM_s V_c N_c}} \propto \frac{1}{\sqrt{N_s}}, \quad (14)$$

when there is zero frequency nonlinearity in the auto-oscillators ($\nu = \beta_m = 0$) and zero detuning between the central frequency of the magnetic cells and the *LCR* resonator ($\bar{\omega} = \omega_r$). In Appendix C, we further verify that $b_{rf,c} \propto 1/\sqrt{N_s}$ holds for the more general case where the nonlinear frequency shift of the magnetic cells and a finite detuning are taken into account ($d\omega_i/dp_i \neq 0$, $\bar{\omega} \neq \omega_r$). Choosing parameters ($\Delta_m$, $\delta\omega = \bar{\omega} - \omega_r$, and β_m) that are consistent with our simulated materials (Appendix D), we calculate $b_{rf,c}$ using the full analytical model and obtain the red curve in Fig. 3(c), which agrees well with the micromagnetic simulation results (solid dots).

Besides the threshold coupling strength, the amplitude of the *LCR* resonator c_r in the synchronized state can also be derived analytically (Appendix C). With the same parameter set that determines $b_{\mathrm{rf,c}}$, we calculate the stored energy in the *LCR* resonator $E_r = L|c_r|^2/2$, as represented by the red curve in Fig. 3(d), consistent with the numerical simulation results, where E_r scales with N_s.

D. Simulation results on oscillation linewidth

One of the key benefits of coupling auto-oscillators with a cavity is to obtain very narrow linewidths. To evaluate the generation linewidth of our proposed device at finite temperature, we carry out micromagnetic simulation at $T = 300$ K. We note that compared with the $T = 0$ K case shown in Fig. 3(c), the required coupling coefficient $b_{\mathrm{rf,c}}$ increases by 20% but the synchronization and phase-locking behaviors remain. The resolution of the oscillation linewidth is determined by the simulated evolution time for magnetization, which is further limited by the hardware and software efficiency. For a sample with $D = 5120$ nm, an upper bound of 4 kHz is determined for the linewidth of voltage (full width at half maximum, or FWHM) after 35 days of simulation, as shown in Fig. 4(a). The quality of the generation signal ($Q_g > 10^6$) is much higher than the intrinsic quality factor of the *LCR* resonator ($Q = 10^3$), which suggests that the narrow linewidth does not originate from the simple filtering effect of the resonator. To gain a better understanding on the generation linewidth as a function of the device size, we perform simulations on a series of samples and the results are summarized in Fig. 4(b). It can be seen that the linewidth Δf reduces as N_s increases, satisfying a relationship $\Delta f \propto 1/N_s$ (red curve), which suggests that an even narrower linewidth than shown in Fig. 4 can potentially be achieved in real samples with larger dimensions.

This scaling trend is consistent with the theory on thermal-phase-noise-induced auto-oscillator linewidth broadening [26,27], where it has been shown that $\Delta f \propto k_B T/E$, where E is the oscillation energy of the system. In our system, the total energy contains both the resonator energy and the energy of the magnetization oscillation [26,27], both of which are proportional to N_s. The analytical understanding of the linewidth and the simulations beyond white noise, such as the $1/f$ noise in the coupled system [26,55], are important future research directions.

III. DISCUSSION AND CONCLUSIONS

The proposed device structure can not only be used as a general-purpose on-chip microwave source but also provides important functionalities in emerging fields such as quantum electronics. In the field of quantum engineering, a scalable approach for interconnecting quantum bits with high-quality microwave sources is required for realizing large-scale quantum processors [56]. The STO maser discussed in this paper is a compact highly coherent microwave source that can be realized using a scalable photolithography process [41,42]. The oscillator is already coupled with photon mode of the cavity, which can provide direct output to other parts of the quantum circuits. Moreover, with a modulated dc spin current, the STO maser can generate high-quality microwave pulses with controlled envelopes, which holds potential for applications in scalable quantum information processing.

In summary, we study the dynamics of a multidomain STO located within a microwave resonator. We find that, different from free STOs, a STO coupled with a microwave resonator can exhibit coherent oscillations even in large extended ferromagnetic thin films. In the coherent region, the microwave emission power increases with the dimension of the magnetic film, while the generation linewidth reduces. The requirement for reaching the coherent region can be satisfied by increasing the volume of the magnetic films and using a two-dimensional resonator design that can be achieved with existing technologies. The operation mechanism of this device is reminiscent of a maser, with a large-area STO serving as the nonlinear gain medium. Although the system is described by classical dynamical equations without referring to quantized energy levels, we note that essential laser physics can be understood in classical physics [44], with examples of free-electron lasers [57,58] and Josephson-junction lasers [59,60]. By harnessing spin-photon coupling and spin-orbit torque, we expect that the demonstrated results can enable compact highly coherent on-chip microwave sources that are beneficial for applications in both the classical and the quantum electronics domain.

FIG. 4.   (a) The Fourier transform of resonator voltage V for samples with $D = 640$, 1280, and 5120 nm. The red curves for the $D = 640$ and 1280 nm samples illustrate Lorentzian fittings. (b) The voltage FWHM linewidth as a function of the diameter D. To ensure fair comparisons, $b_{\mathrm{rf}}D$ is kept constant in simulating samples with different sizes, with $b_{\mathrm{rf}} = 15$ T/A for $D = 1280$ nm. In this simulation, $T = 300$ K and the lateral size of cells is chosen to be 10 nm.

APPENDIX A: THERMAL NOISE FOR MICROMAGNETIC SIMULATIONS WITH A MICROWAVE RESONATOR

In this appendix, we provide derivations of the thermal-noise terms in Eqs. (1)–(3). In the main text, we show that the dynamical equations for each magnetic cell i within a magnetic film and the serial LCR circuit with the mutual coupling terms can be written as

$$\frac{d\hat{\mathbf{m}}_i}{dt} = \boldsymbol{\tau}_i - \gamma\hat{\mathbf{m}}_i \times \mathbf{b_{rf}}I, \tag{A1}$$

$$\frac{dI}{dt} = \frac{V}{L} - \frac{R}{L}I - \frac{b_{rf}M_sV_c}{L}\sum_i \frac{d\hat{m}_{xi}}{dt}, \tag{A2}$$

$$\frac{dV}{dt} = -\frac{I}{C}. \tag{A3}$$

To consider the finite-temperature effect, the agitation from thermal noise should be included in the dynamics of the magnet and the LCR resonator. For the magnetic dynamics, we use the torque from the thermal effect that is included in the standard MUMAX3 package [46]. For the LCR resonator, we define a complex amplitude $c_r = \sqrt{p_r}e^{i\phi_r} = I + iV/Z$, where $Z = \sqrt{L/C}$ is the characteristic impedance. Equations (A2) and (A3) without the coupling term can then be combined into a single equation $(dc_r/dt) = -i\omega_r c_r - (R/2L)c_r + f_r(t)$, with a complex thermal-noise term $f_r(t)$, where $\omega_r = 1/\sqrt{LC}$ is the resonance frequency (nonresonant terms proportional to c_r^* are dropped). Following Slavin et al. [1], we consider Gaussian white noise such that $\langle f_r(t)f_r(t')\rangle = 0$ and $\langle f_r(t)f_r^*(t')\rangle = 2D_r\delta(t - t')$, where D_r is the diffusion coefficient. Under the Fokker-Planck equation, the stationary probability density function $\mathcal{P}_r(p_r, \phi_r, t)$ satisfies $(d/dp_r)[2p_r(R/2L)\mathcal{P}_r + 2p_rD_r(\partial\mathcal{P}_r/\partial p_r)] = 0$ [1]. In the meantime, $\mathcal{P}_r$ needs to satisfy the Boltzmann distribution under thermal equilibrium at temperature T, $\mathcal{P}_r \propto e^{-E_r/k_BT}$, where $E_r = CV^2/2 + LI^2/2 = Lp_r/2$ is the energy stored in the resonator. This sets $D_r = Rk_BT/L^2$. Rewriting the thermal-noise terms for c_r into equations in terms of I and

V, we obtain

$$\frac{d\hat{\mathbf{m}}_i}{dt} = \boldsymbol{\tau}_i - \gamma\hat{\mathbf{m}}_i \times \mathbf{b_{rf}}I, \tag{A4}$$

$$\frac{dI}{dt} = \frac{V}{L} - \frac{R}{L}I - \frac{b_{rf}M_sV_c}{L}\sum_i \frac{d\hat{m}_{xi}}{dt} + f_I(t), \tag{A5}$$

$$\frac{dV}{dt} = -\frac{I}{C} + f_V(t), \tag{A6}$$

where $\langle f_I(t)f_I(t')\rangle = Rk_BT/L^2\delta(t - t')$ and $\langle f_V(t)f_V(t')\rangle = Rk_BT/LC\delta(t - t')$, respectively.

APPENDIX B: THEORY OF NONLINEAR AUTO-OSCILLATOR COUPLED WITH LINEAR RESONATOR

For this appendix, we consider a STO modeled as a macrospin, which is coupled to an LCR resonator at $T = 0$ K as described by Eqs. (A1)–(A3). The results from this appendix are used as a basis for the derivation of the synchronization condition for coupling multidomain oscillators with a resonator. Here, we first recap some of the key results for a STO without spin-photon coupling given by Slavin et al. [50] and consider the effects of coupling terms later. For a macrospin with magnetic moment $\mathbf{M}$ per unit volume (magnetization), the LLG equation with a spin-transfer term can be written as

$$\frac{d\mathbf{M}}{dt} = \gamma\left(\mathbf{M} \times \frac{\delta W_0}{\delta\mathbf{M}}\right) + \mathbf{T}_\epsilon. \tag{B1}$$

Here, $W_0 = \int[-\mathbf{H}_0 \cdot \mathbf{M} + 2\pi(\mathbf{M} \cdot \hat{\mathbf{z}})^2 - (H_a/2M_s)(\mathbf{M} \cdot \hat{\mathbf{z}})^2]d\mathbf{r}$ is the free energy, with H_a being the anisotropy field, and $\mathbf{T}_\epsilon = \mathbf{T}_h + \mathbf{T}_d + \mathbf{T}_s$ includes contributions from the external microwave field $\mathbf{T}_h = -\gamma(\mathbf{M} \times \mathbf{h})$, Gilbert damping $\mathbf{T}_d = (\alpha/M_s)[\mathbf{M} \times (\partial\mathbf{M}/\partial t)]$, and spin torque $\mathbf{T}_s = (\beta J_s/M_s)[\mathbf{M} \times (\mathbf{M} \times \hat{\mathbf{p}})]$, where $\beta = (g\mu_B/2eM_st)$, with t being the thickness of the magnetic film and J_s being the spin-current density. Here, we consider $\mathbf{H}_0 = H_0\hat{\mathbf{y}}$, $\mathbf{h} = h_x\hat{\mathbf{x}}$, and that the injected spin moments are oriented along the $-y$ axis. Due to the fixed-length constraint $|\mathbf{M}| = M_s$, there are two independent degrees of freedom, which can be conveniently described by a complex circular precession amplitude a_m given by the Holstein-Primakoff transformation $a_m = (M_z - iM_x)/\sqrt{2M_s(M_s + M_y)}$. The inverse transformation is $\mathbf{M} = M_s(1 - 2|a_m|^2)\hat{\mathbf{y}} + M_s\sqrt{1 - |a_m|^2}[(\hat{\mathbf{z}} + i\hat{\mathbf{x}})a_m + (\hat{\mathbf{z}} - i\hat{\mathbf{x}})a_m^*]$. Clearly, only a_m values satisfying $|a_m| \leq 1$ have physical meaning. The equation of motion (EOM) can be written as

$$\frac{da_m}{dt} = -i\frac{\delta\mathcal{H}_0}{\delta a_m^*} + F_a, \tag{B2}$$

where $\mathcal{H}_0 = \gamma W_0/2M_s$ is the macrospin Hamiltonian and $F_a = (\partial a_m/\partial\mathbf{M}) \cdot \mathbf{T}_\epsilon$. Because of the elliptical orbit of

magnetization precession, the Hamiltonian will take a simpler form in elliptical precession amplitudes, called b_m. The relation between the a_m and b_m amplitudes is $a_m = ub_m - vb_m^*$ with $u = \sqrt{(\omega_H + \omega_0)/2\omega_0}$ and $v = \sqrt{(\omega_H - \omega_0)/2\omega_0}$, where $\omega_H = \gamma(H_0 + 2\pi M_{\text{eff}})$ and $\omega_0 = \gamma\sqrt{H_0(H_0 + 4\pi M_{\text{eff}})}$ with $4\pi M_{\text{eff}} = 4\pi M_s - H_a$. This is a canonical transformation analogous to Bogoliubov transformation. In terms of b_m, the EOM is

$$\frac{db_m}{dt} = -i\frac{\delta\mathcal{H}_0}{\delta b_m^*} + F_b, \quad (B3)$$

where $F_b = uF_a + vF_a^*$. Following the convention utilized in Slavin *et al.* [50], a new complex amplitude $c_m = \sqrt{\omega_H/\omega_0}b_m$ is defined, where subscript m denotes magnetic dynamics, to distinguish this from the resonator dynamics introduced later. By neglecting nonresonant terms and keeping leading-order terms, we finally write the EOM in terms of c_m:

$$\frac{dc_m}{dt} = -i\frac{\delta\mathcal{H}_c}{\delta c_m^*} - \Gamma_+(|c_m|^2)c_m + \Gamma_-(|c_m|^2)c_m + F_{ch}. \quad (B4)$$

Here, $\mathcal{H}_c = \omega_H\mathcal{H}_0/\omega_0 = \omega_0|c_m|^2 + (K/2)|c_m|^4$, with $\omega_0|c_m|^2$ being the linear term and $(K/2)|c_m|^4$ corresponding to the nonlinear frequency shift, $K = \gamma(2\omega_0/\omega_H)\{-[3(u^2 + v^2)^2 - 1] + 6uv(u^2 + v^2)\}\pi M_{\text{eff}}$. The second and third terms on the right-hand side of Eq. (B4) represent the positive nonlinear damping $\Gamma_+(|c_m|^2) = \Gamma_0(1 + Q_1|c_m|^2 + Q_2|c_m|^4)$ due to Gilbert damping and negative nonlinear damping $\Gamma_-(|c_m|^2) = \Gamma_J(1 - |c_m|^2)$ due to the spin-torque effect, with $\Gamma_0 = \alpha\omega_H$, $\Gamma_J = \beta J_s$, $Q_1 = 2 - 3(\omega_0/\omega_H)^2 - 2\omega_H'/\omega_H$, and $Q_2 = [2 - 3(\omega_H'/\omega_H) + (\omega_H'/\omega_H)^2](\omega_H'/\omega_H)$, with $\omega_H' = \gamma 2\pi M_{\text{eff}}$. In the following discussions, we consider the case with $\Gamma_J > \Gamma_0$, corresponding to the operation regime of STOs. The external microwave field effect contributes to an additional driving term $F_{ch} = \gamma\sqrt{\omega_H/\omega_0}(u + v)h_x/2$, up to leading order. These results are adapted from Slavin *et al.* [50] after considering our proposed device geometry.

In the following, we consider the coupling between the macrospin STO and the *LCR* circuit, which is a coupling scheme raised in the current work and has not been visited in previous publications. We first note that the effect of the *LCR* circuit on macrospin is to produce an effective magnetic field $\mathbf{h} = h_x\hat{\mathbf{x}} = b_{\text{rf}}I\hat{\mathbf{x}}$, resulting in $F_{ch} = \gamma\sqrt{\omega_H/\omega_0}(u + v)(c_r + c_r^*)b_{\text{rf}}/4$, where $c_r = I + iV/Z$ is the complex resonator amplitude defined in the previous appendix. To consider the effect of STO dynamics on the *LCR* resonator, we rewrite Eqs. (A2) and (A3) using c_r:

$$\frac{dc_r}{dt} = -i\omega_r c_r - \frac{R}{2L}c_r - \frac{b_{\text{rf}}}{L}\frac{dm_x}{dt}, \quad (B5)$$

where $\omega_r = 1/\sqrt{LC}$ (terms proportional to c_r^* are dropped). Since m_x is correlated with c_m through the transformations introduced above, we can rewrite $(dm_x/dt) = iM_sV_c(u + v)\sqrt{\frac{\omega_0}{\omega_H}}[(dc_m/dt) - (dc_m^*/dt)]$ up to leading order, where V_c is the volume of the macrospin cell. Substituting the expressions for F_{ch} and (dm_x/dt) into Eqs. (B4) and (B5) and only keeping leading-order terms, we obtain equations that describe the dynamics of the coupled system regarding the two complex amplitudes c_m and c_r:

$$\frac{dc_m}{dt} + i\omega(|c_m|^2)c_m + \Gamma(|c_m|^2)c_m = F_m(c_r), \quad (B6)$$

$$\frac{dc_r}{dt} + i\omega_r c_r + \frac{\omega_r}{2Q}c_r = F_r(c_m), \quad (B7)$$

where $\Gamma(|c_m|^2) = \Gamma_+(|c_m|^2) - \Gamma_-(|c_m|^2)$, $\omega(|c_m|^2) = \omega_0 + K|c_m|^2$, $F_m(c_r) = g_m c_r$, $F_r(c_m) = -g_r c_m$, and $Q = \sqrt{L/C}/R$ is the quality factor of the *LCR* resonator. The parameters for the coupling terms are $g_m = \gamma b_{\text{rf}}/4$ and $g_r = \omega_0 b_{\text{rf}}M_sV_c/L$. In Eqs. (B6) and (B7), we drop terms proportional to c_m^* and c_r^* under the rotating-wave approximation [50]. In the main text, we consider the case where the demagnetization field is nearly compensated with the perpendicular anisotropy, therefore, we set $\omega_H \approx \omega_0$ and $u + v = 1$ in the equations above. We note that $g_m \propto b_{\text{rf}}$ and $g_r \propto b_{\text{rf}}N_s$, where N_s is the number of spins. Equations (B6) and (B7) represent coupling between a nonlinear auto-oscillator and a linear passive resonator, different from mutual synchronization between two STOs (nonlinear auto-oscillators) in the previous literature [1]. To proceed, by expressing $c_m = \sqrt{p_m}e^{i\phi_m}$ and $c_r = \sqrt{p_r}e^{i\phi_r}$, we separate Eqs. (B6) and (B7) into equations about the magnitude and about the phase:

$$\frac{dp_m}{dt} + 2\Gamma(p_m)p_m = 2g_m\sqrt{p_r p_m}\cos(\phi_r - \phi_m), \quad (B8)$$

$$\frac{d\phi_m}{dt} + \omega(p_m) = g_m\sqrt{\frac{p_r}{p_m}}\sin(\phi_r - \phi_m), \quad (B9)$$

$$\frac{dp_r}{dt} + \frac{\omega_r}{Q}p_r = -2g_r\sqrt{p_r p_m}\cos(\phi_r - \phi_m), \quad (B10)$$

$$\frac{d\phi_r}{dt} + \omega_r = g_r\sqrt{\frac{p_m}{p_r}}\sin(\phi_r - \phi_m). \quad (B11)$$

Without the coupling term, which is proportional to g_m, the relevant solution to Eqs. (B8) and (B9) is the persistent macrospin precession with stationary power p_0 satisfying $\Gamma_+(p_0) = \Gamma_-(p_0)$ and generation frequency $\omega_g = \omega(p_0)$. In the limit of weak coupling, we can expand Eqs. (B8) and (B9) around the stationary point by treating power

deviation $\delta p_m = p_m - p_0$ as a small signal [1]:

$$\frac{d\delta p_m}{dt} + 2\Gamma_p \delta p_m = 2g_m \sqrt{p_r p_0} \cos(\phi_r - \phi_m), \quad \text{(B12)}$$

$$\frac{d\phi_m}{dt} + \omega_g + K\delta p_m = g_m \sqrt{\frac{p_r}{p_0}} \sin(\phi_r - \phi_m), \quad \text{(B13)}$$

where $\Gamma_p = (G_+ - G_-)p_0$ with $G_+ = (d\Gamma_+/dp)|_{p_0}$ and $G_- = (d\Gamma_-/dp)|_{p_0}$. Defining $\nu = K/(G_+ - G_-)$ and keeping leading-order terms, the dynamics of Eqs. (B8)–(B11) can be captured by the following equations:

$$\frac{d\phi_m}{dt} + \omega_g = g_m\sqrt{1+\nu^2}\sqrt{\frac{p_r}{p_0}} \sin(\phi_r - \phi_m - \beta_m),$$
$$\text{(B14)}$$

$$\frac{d\phi_r}{dt} + \omega_r = g_r\sqrt{\frac{p_0}{p_r}} \sin(\phi_r - \phi_m), \quad \text{(B15)}$$

$$\frac{dp_r}{dt} + \frac{\omega_r}{Q}p_r = -2g_r\sqrt{p_r p_0}\cos(\phi_r - \phi_m), \quad \text{(B16)}$$

where $\beta_m = \arctan(\nu)$ is a phase due to nonlinear frequency shift. Equations (B14)–(B16) serve as a basis for deriving the synchronization condition in a resonator-coupled multidomain STO in Appendix C. Moreover, this macrospin theory also describes the STO maser in the synchronized region with $b_{\rm rf} \geq b_{\rm rf,c}$, as discussed below.

We seek a stationary solution where $dp_r/dt = 0$, which suggests that $\cos(\phi_r - \phi_m) < 0$ and $\Phi = \phi_r - \phi_m$ is a constant in time, indicating phase locking. Then we have

$$p_r = 4p_0 \left[g_r \frac{Q}{\omega_r} \cos\Phi \right]^2, \quad \text{(B17)}$$

$$\omega_r - \omega_g = -\frac{\omega_r}{2Q}\tan\Phi + 2G\frac{Q}{\omega_r}\cos\Phi\sin(\Phi - \beta_m),$$
$$\text{(B18)}$$

where $G = g_m g_r \sqrt{1+\nu^2}$. Equation (B18) determines the stationary locked phase Φ, which then determines resonator power p_r in Eq. (B17). Note that $g_m \propto b_{\rm rf}$ and $g_r \propto b_{\rm rf}N_s$. Therefore, the locked phase Φ depends on $b_{\rm rf}$ and N_s through $G \propto b_{\rm rf}^2 N_s$. In our simulations, $a_m \approx c_m$ due to the nearly compensated magnetic anisotropy and we approximate $\phi_m = \arctan(-\langle\hat{m}_x\rangle/\langle\hat{m}_z\rangle)$. The locked phases Φ as a function of the diameter D and $b_{\rm rf}$ are extracted from the simulation and plotted in Fig. 5. We note that $\cos\Phi < 0$ and that Φ depends on $b_{\rm rf}$ and N_s through the combination $b_{\rm rf}D \propto b_{\rm rf}N_s^2$, as illustrated in Fig. 5(b), consistent with the macrospin theory.

Besides, we can obtain the microwave emission frequency by inserting Eq. (B17) into Eq. (B15), obtaining $(d\phi_r/dt) = -\omega_r[1 + \tan(\Phi)/2Q]$. This indicates a relation
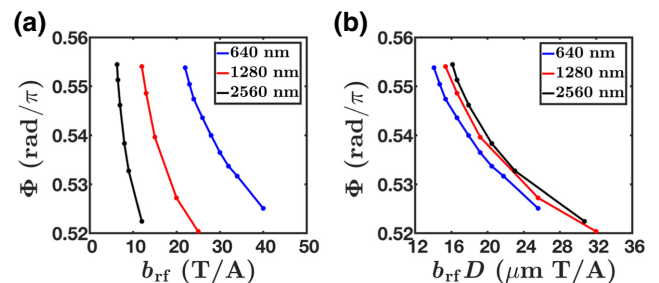

FIG. 5. The locked phase $\Phi = \phi_r - \phi_m$ as a function of (a) $b_{\rm rf}$ and (b) $b_{\rm rf}D$ for different diameters D, with $b_{\rm rf} \geq b_{\rm rf,c}$. In this simulation, $T = 0$ K and the lateral size of cells is chosen to be 2.5 nm.

between the phase-locked frequency and the phase:

$$\omega_{PL} = \omega_r\left(1 + \frac{1}{2Q}\tan\Phi\right). \quad \text{(B19)}$$

In Fig. 6, the theoretical phase-locked frequencies calculated using Eq. (B19) and phases in Fig. 5 are shown as solid curves, which agree well with the peak frequencies obtained from simulation, represented by pentagram dots.

APPENDIX C: SYNCHRONIZATION CONDITION FOR MULTIDOMAIN SPIN-TORQUE OSCILLATOR WITH MICROWAVE RESONATOR

We model the multidomain STO as consisting of N_c magnetic cells with volume V_c. As shown in the earlier literature, in the limit of large N_c, short-range interactions such as nearest-neighbor interaction from exchange and power-law interaction from the dipolar field are insufficient to achieve the synchronization of different cells. Moreover, it is mathematically challenging to derive an analytical solution for the synchronization in the presence
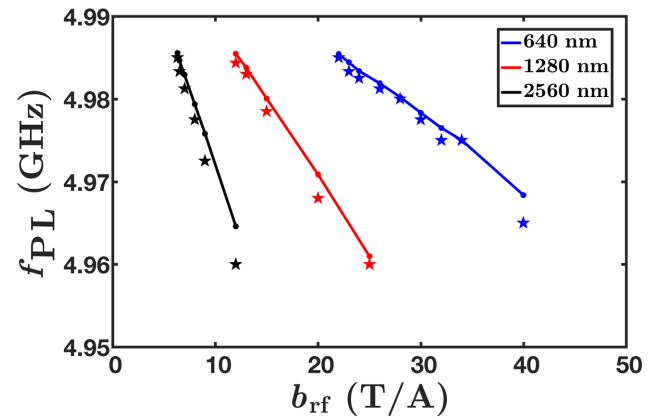

FIG. 6. The phase-locked frequency $f_{\rm PL}$ with $b_{\rm rf} \geq b_{\rm rf,c}$. The pentagram dots represent the peak frequencies extracted from simulation. The solid curves represent calculations using macrospin theory and the locked phases presented in Fig. 5.

of these short-range coupling terms. Here, we only consider the interaction between the magnetic cells and the *LCR* resonator. We show below that this model captures the features of our simulation results semiquantitatively. The dynamical equations of the system at $T = 0$ K are the generalization of Eqs. (B6) and (B7):

$$\frac{dc_i}{dt} + i\omega_i(|c_i|^2)c_i + \Gamma_{+i}(|c_i|^2)c_i - \Gamma_{-i}(|c_i|^2)c_i = F_{mi}(c_r),$$

(C1)

$$\frac{dc_r}{dt} + i\omega_r c_r + \frac{\omega_r}{2Q}c_r = \sum_i F_{ri}(c_i),$$

(C2)

where i is the cell index. In general, the functions ω_i, Γ_{+i}, Γ_{-i}, F_{mi}, and F_{ri} have i-dependent functional forms due on spatial variation of the equilibrium effective field. For each unit cell with complex amplitude $c_i = \sqrt{p_i}e^{i\phi_i}$, one can expand the equation around the stationary working point with corresponding stationary power p_{i0} and generation frequency ω_{gi}, as we do in Eq. (B14):

$$\frac{d\phi_i}{dt} + \omega_{gi} = g_m\sqrt{1+v_i^2}\sqrt{\frac{p_r}{p_{i0}}} \sin(\phi_r - \phi_i - \beta_i),$$ (C3)

$$\frac{dc_r}{dt} + i\omega_r c_r + \frac{\omega_r}{2Q}c_r = \sum_i -g_{ri}\sqrt{p_{i0}}e^{i\phi_i},$$ (C4)

where the definitions of g_{mi}, v_i, and β_i are in line with the corresponding definitions of g_m, v, and β_m in Appendix B. These equations describe a complicated dynamical system with dimension $N_c + 2$. To obtain the qualitative features of the system, we set all parameters except ω_{gi} to their average values $v_i = v$, $p_{i0} = p_0$, $\beta_i = \beta_m$, and $g_{ri} = g_r$. In the limit of large N_c, we assume that the frequency and phase distribution of the magnetic cells satisfy a probability function $f(\phi, \omega, t)$, where $f(\phi, \omega, t)d\phi d\omega$ describes the fraction of cells in phase $(\phi, \phi + d\phi)$ and frequency $(\omega, \omega + d\omega)$ [53]. We define the phase order parameter,

$$\Psi = \frac{1}{N_c}\sum_i e^{i\phi_i} = \int_{-\infty}^{\infty} d\omega \int_0^{2\pi} f(\phi, \omega, t)e^{i\phi}d\phi,$$ (C5)

and we can rewrite Eqs. (C3) and (C4) as

$$\frac{d\phi}{dt} + \omega = g_m\sqrt{1+v^2}\sqrt{\frac{p_r}{p_0}} \sin(\phi_r - \phi - \beta_m),$$ (C6)

$$\frac{dc_r}{dt} + i\omega_r c_r + \frac{\omega_r}{2Q}c_r = -g_r\sqrt{p_0}N_c\Psi.$$ (C7)

The function $f(\phi, \omega, t)$ satisfies the continuity equation $(\partial f/\partial t) + \partial_\phi(f\dot{\phi}) = 0$, where $\dot{\phi}$ is given by Eq. (C6).

Following the Ott-Antonsen ansatz [53,54], we have a tentative solution $f(\phi, \omega, t)$ expressed in a Fourier series:

$$f(\phi, \omega, t) = \frac{h(\omega)}{2\pi}\left[1 + \sum_{n=1}^{\infty}[\alpha(\omega, t)]^n e^{in\phi} + c.c.\right],$$ (C8)

where the Fourier coefficients take the functional form of $[\alpha(\omega, t)]^n$, which is used to describe systems with a large number of oscillators. We note that $h(\omega) = \int_0^{2\pi} f(\phi, \omega, t)d\phi$ is the distribution of the generation frequency of magnetic cells. Substituting Eqs. (C8) and (C6) into the continuity equation, we have

$$\frac{\partial\alpha}{\partial t} - i\omega\alpha$$
$$= \frac{g_m\sqrt{(1+v^2)p_r}}{2\sqrt{p_0}}\left[e^{-i(\phi_r - \beta_m)} - \alpha^2 e^{i(\phi_r - \beta_m)}\right].$$ (C9)

Moreover, within the Ott-Antonsen ansatz, we note that the phase order parameter can be written as $\Psi = \int_{-\infty}^{\infty} d\omega h(\omega)\alpha^*(\omega, t)$. In order to obtain qualitative results, we assume that the frequency distribution follows the Lorentzian distribution $h(\omega) = (\Delta_m/\pi)[(\omega - \bar{\omega})^2 + \Delta_m^2]^{-1}$, which would simplify the expression of the phase order parameter to $\Psi = [\alpha(\bar{\omega} + i\Delta_m, t)]^*$, using contour integration in the upper half complex plane [53]. As a result, Eq. (C9) governs the time evolution of Ψ, which, together with Eq. (C7), specifies the dynamics of the system:

$$\frac{\partial\Psi}{\partial t} + i(\bar{\omega} - i\Delta_m)\Psi = \frac{g_m\sqrt{1+v^2}}{2\sqrt{p_0}}\left[c_r e^{-i\beta_m} - \Psi^2 c_r^* e^{i\beta_m}\right].$$

(C10)

To proceed, we write $\Psi = \Psi_0 e^{i\phi_0}$, where the phase ϕ_0 denotes the phase of the order parameter for magnetic dynamics. We separate Eqs. (C10) and (C7) into phase and amplitude parts:

$$\frac{d\Psi_0}{dt} = -\Delta_m\Psi_0 + G_m\left(\frac{1-\Psi_0^2}{2}\right)\cos(\phi_r - \phi_0 - \beta_m),$$

(C11)

$$\frac{d\phi_0}{dt} + \bar{\omega} = G_m\left(\frac{1+\Psi_0^2}{2}\right)\sin(\phi_r - \phi_0 - \beta_m),$$ (C12)

$$\frac{dp_r}{dt} + \frac{\omega_r}{Q}p_r = -2g_r\sqrt{p_r p_0}N_c\Psi_0\cos(\phi_r - \phi_0),$$ (C13)

$$\frac{d\phi_r}{dt} + \omega_r = g_r\sqrt{\frac{p_0}{p_r}}N_c\Psi_0\sin(\phi_r - \phi_0),$$ (C14)

where $G_m = g_m\sqrt{1+\nu^2}\sqrt{(p_r/p_0)}$. We note that Eqs. (C12)–(C14) generalize Eqs. (B14)–(B16), and that they become identical in the case of $\Psi_0 = 1$, consistent with the macrospin picture. The parameter g_r in Eqs. (C13)–(C14) represents coupling from a single magnetic cell, which is accompanied by the number of cells N_c accounting for proper size scaling. Equation (C11) is a new equation that quantifies the coherence of magnetic dynamics. In the absence of coupling to the resonator ($g_m = 0$), one can verify that $\Psi_0 = 0$ is a stable solution, corresponding to complete incoherence. However, as described below, when the mutual coupling strength represented by $g_m g_r N_c$ reaches a critical value, this incoherence solution will lose its stability and the alternative phase-locked solution will describe the long-term dynamics of the hybrid system. To find this phase boundary, we linearize Eq. (C10) near $\Psi_0 = 0$ by discarding the Ψ^2 term. Assuming that $\Psi = \Psi_0 e^{(\lambda - i\Omega)t}$ and $c_r = c_{r0} e^{(\lambda - i\Omega)t}$ in the linearized Eqs. (C7) and (C10), we have

$$[\lambda + \Delta_r - i(\Omega - \omega_r)][\lambda + \Delta_m - i(\Omega - \bar{\omega})]$$
$$= \frac{1}{2} g_m g_r N_c \sqrt{1+\nu^2} e^{-i\beta_m}, \quad \text{(C15)}$$

where $\Delta_r = \omega_r/2Q$ corresponds to the linewidth of the resonator. The phase boundary for the growth of coherence from the $\Psi_0 = 0$ state is given by the condition $\lambda = 0^+$ in Eq. (C15), which can be reached by a certain critical value of $g_m g_r N_c$. We define the corresponding threshold $b_{\rm rf}$ value as $b_{{\rm rf},c}$. Under $\lambda = 0^+$, by letting the real and imaginary parts on both sides of Eq. (C15) equal each other, we arrive at the following equation for $b_{{\rm rf},c}$:

$$\frac{\left[\delta\omega\Delta_r - \frac{1}{2}G(b_{{\rm rf},c})\sin\beta_m\right]\left[\delta\omega\Delta_m + \frac{1}{2}G(b_{{\rm rf},c})\sin\beta_m\right]}{(\Delta_m + \Delta_r)^2}$$
$$= -\frac{1}{2}G(b_{{\rm rf},c})\cos\beta_m - \Delta_r\Delta_m, \quad \text{(C16)}$$

where $\delta\omega = \bar{\omega} - \omega_r$, $G(b_{{\rm rf},c}) = g_{m,c} g_{r,c} N_c \sqrt{1+\nu^2} \propto b_{{\rm rf},c}^2 N_s$, with N_s being the number of total spins. Note that the threshold equation Eq. (C16) depends on $b_{{\rm rf},c}$ and N_s only through $G(b_{{\rm rf},c}) \propto b_{{\rm rf},c}^2 N_s$, which leads to the conclusion that $b_{{\rm rf},c} \propto 1/\sqrt{N_s}$, consistent with the simulation results presented in the main text. Equation (C16) is a generalized result of the famous Millennium Bridge problem by extending it to oscillators with a nonlinear frequency shift, e.g., STOs [1,54,61]. Above the threshold coupling $b_{\rm rf} \geq b_{{\rm rf},c}$, the stationary solution is described by the phase-locked solution with nonzero Ψ_0 given in Eqs. (C11)–(C14). Combining Eqs. (C12) and (C14) by defining $\Phi = \phi_r - \phi_0$, the phase-locked stationary solution is described by

$$\Delta_m = -G(b_{\rm rf})\frac{Q}{\omega_r}(1 - \Psi_0^2)\cos\Phi\cos(\Phi - \beta_m), \quad \text{(C17)}$$

$$\omega_r - \bar{\omega} = -\frac{\omega_r}{2Q}\tan\Phi + Z_0 G(b_{\rm rf})\frac{Q}{\omega_r}\cos\Phi\sin(\Phi - \beta_m), \quad \text{(C18)}$$

$$p_r = 4p_0\left[\Psi_0 g_r N_c\frac{Q}{\omega_r}\cos\Phi\right]^2, \quad \text{(C19)}$$

where $Z_0 = (1 + \Psi_0^2)\Psi_0$. The unknowns in Eqs. (C17)–(C19) are Ψ_0, Φ, and p_r, with $\Delta_m, \bar{\omega}, g$, and β_m being material- and biasing-dependent parameters. Equations (C17)–(C18) depend on $b_{\rm rf}$ through the function $G(b_{\rm rf}) \propto b_{\rm rf}^2 N_s$. As a consequence, Ψ_0 and Φ can be determined from those two equations as functions of $b_{\rm rf}^2 N_s$ when the other parameters are fixed. Therefore, for samples with different dimensions, if we pick $b_{\rm rf}$ slightly above the corresponding threshold value of $b_{{\rm rf},c}$, as we do in Fig. 3(d) of the main text, we will obtain the same Ψ_0 and Φ, since $b_{\rm rf}^2 N_s$ remains a constant. From Eq. (C19), we then obtain $p_r \propto (g_r N_c)^2 \propto (b_{\rm rf}N_s)^2 \propto N_s$, which describes the simulation results presented in the main text.

APPENDIX D: PARAMETER SET IN ANALYTICAL MODEL

With Eqs. (C16)–(C19), the theoretical model explains the simulation results of $b_{{\rm rf},c}$ and $E_r = Lp_r/2$ in the main text. With $L = 1.56$ nH, $M_s = 5.5 \times 10^5$ A/m, and $\omega_0 \approx 2\pi \times 5.44$ GHz utilized in the simulations, the values of $g_m = \gamma b_{\rm rf}/4$ and $g_r N_c = \omega_0 b_{\rm rf} M_s V_c N_c/L$ for different $b_{\rm rf}$ and D can be determined. Moreover, we estimate the value of $p_0 \approx 0.3167$ from simulation of the uncoupled case. Under the chosen optimal parameters of $\Delta_m = 2\pi \times 0.326$ GHz, $\omega_r - \bar{\omega} = 2\pi \times 0.28$ GHz, and $\beta_m = 2.43$, the analytical model gives the red curves in Figs. 3(c) and 3(d) in the main text. For a self-consistency check, $\nu = \tan\beta_m < 0$ gives $K < 0$, which is consistent with the fact that $\bar{\omega} < \omega_0$.

[1] A. Slavin and V. Tiberkevich, Nonlinear auto-oscillator theory of microwave generation by spin-polarized current, IEEE Trans. Magn. **45**, 1875 (2009).

[2] T. Chen, R. K. Dumas, A. Eklund, P. K. Muduli, A. Houshang, A. A. Awad, P. Dürrenfeld, B. G. Malm, A. Rusu, and J. Åkerman, Spin-torque and spin-hall nano-oscillators, Proc. IEEE **104**, 1919 (2016).

[3] S. I. Kiselev, J. C. Sankey, I. N. Krivorotov, N. C. Emley, R. J. Schoelkopf, R. A. Buhrman, and D. C. Ralph, Microwave oscillations of a nanomagnet driven by a spin-polarized current, Nature **425**, 380 (2003).

[4] W. H. Rippard, M. R. Pufall, S. Kaka, S. E. Russek, and T. J. Silva, Direct-Current Induced Dynamics in $Co_{90}Fe_{10}/Ni_{80}Fe_{20}$ Point Contacts, Phys. Rev. Lett. **92,** 027201 (2004).

[5] I. N. Krivorotov, N. C. Emley, J. C. Sankey, S. I. Kiselev, D. C. Ralph, and R. A. Buhrman, Time-domain measurements of nanomagnet dynamics driven by spin-transfer torques, Science **307,** 228 (2005).

[6] A. A. Tulapurkar, Y. Suzuki, A. Fukushima, H. Kubota, H. Maehara, K. Tsunekawa, D. D. Djayaprawira, N. Watanabe, and S. Yuasa, Spin-torque diode effect in magnetic tunnel junctions, Nature **438,** 339 (2005).

[7] J. Torrejon, M. Riou, F. A. Araujo, S. Tsunegi, G. Khalsa, D. Querlioz, P. Bortolotti, V. Cros, K. Yakushiji, A. Fukushima, H. Kubota, S. Yuasa, M. D. Stiles, and J. Grollier, Neuromorphic computing with nanoscale spintronic oscillators, Nature **547,** 428 (2017).

[8] M. Romera, P. Talatchian, S. Tsunegi, F. Abreu Araujo, V. Cros, P. Bortolotti, J. Trastoy, K. Yakushiji, A. Fukushima, H. Kubota, S. Yuasa, M. Ernoult, D. Vodenicarevic, T. Hirtzlin, N. Locatelli, D. Querlioz, and J. Grollier, Vowel recognition with four coupled spin-torque nano-oscillators, Nature **563,** 230 (2018).

[9] A. M. Deac, A. Fukushima, H. Kubota, H. Maehara, Y. Suzuki, S. Yuasa, Y. Nagamine, K. Tsunekawa, D. D. Djayaprawira, and N. Watanabe, Bias-driven high-power microwave emission from MgO-based tunnel magnetoresistance devices, Nat. Phys. **4,** 803 (2008).

[10] D. Houssameddine, U. Ebels, B. Delaët, B. Rodmacq, I. Firastrau, F. Ponthenier, M. Brunet, C. Thirion, J.-P. Michel, L. Prejbeanu-Buda, M.-C. Cyrille, O. Redon, and B. Dieny, Spin-torque oscillator using a perpendicular polarizer and a planar free layer, Nat. Mater. **6,** 447 (2007).

[11] V. S. Pribiag, I. N. Krivorotov, G. D. Fuchs, P. M. Braganca, O. Ozatay, J. C. Sankey, D. C. Ralph, and R. A. Buhrman, Magnetic vortex oscillator driven by d.c. spin-polarized current, Nat. Phys. **3,** 498 (2007).

[12] I. M. Miron, K. Garello, G. Gaudin, P.-J. Zermatten, M. V. Costache, S. Auffret, S. Bandiera, B. Rodmacq, A. Schuhl, and P. Gambardella, Perpendicular switching of a single ferromagnetic layer induced by in-plane current injection, Nature **476,** 189 (2011).

[13] L. Liu, C.-F. Pai, Y. Li, H. W. Tseng, D. C. Ralph, and R. A. Buhrman, Spin-torque switching with the giant Spin hall effect of tantalum, Science **336,** 555 (2012).

[14] V. E. Demidov, S. Urazhdin, H. Ulrichs, V. Tiberkevich, A. Slavin, D. Baither, G. Schmitz, and S. O. Demokritov, Magnetic nano-oscillator driven by pure spin current, Nat. Mater. **11,** 1028 (2012).

[15] L. Liu, C.-F. Pai, D. C. Ralph, and R. A. Buhrman, Magnetic Oscillations Driven by the Spin Hall Effect in 3-Terminal Magnetic Tunnel Junction Devices, Phys. Rev. Lett. **109,** 186602 (2012).

[16] V. E. Demidov, S. Urazhdin, E. R. J. Edwards, M. D. Stiles, R. D. McMichael, and S. O. Demokritov, Control of Magnetic Fluctuations by Spin Current, Phys. Rev. Lett. **107,** 107204 (2011).

[17] A. Smith, K. Sobotkiewich, A. Khan, E. A. Montoya, L. Yang, Z. Duan, T. Schneider, K. Lenz, J. Lindner, K. An, X. Li, and I. N. Krivorotov, Dimensional crossover in spin hall oscillators, Phys. Rev. B **102,** 054422 (2020).

[18] Z. Duan, A. Smith, L. Yang, B. Youngblood, J. Lindner, V. E. Demidov, S. O. Demokritov, and I. N. Krivorotov, Nanowire spin torque oscillator driven by spin orbit torques, Nat. Commun. **5,** 5616 (2014).

[19] J. Grollier, V. Cros, and A. Fert, Synchronization of spin-transfer oscillators driven by stimulated microwave currents, Phys. Rev. B **73,** 060409(R) (2006).

[20] S. Tsunegi, T. Taniguchi, R. Lebrun, K. Yakushiji, V. Cros, J. Grollier, A. Fukushima, S. Yuasa, and H. Kubota, Scaling up electrically synchronized spin torque oscillator networks, Sci. Rep. **8,** 13475 (2018).

[21] S. Kaka, M. R. Pufall, W. H. Rippard, T. J. Silva, S. E. Russek, and J. A. Katine, Mutual phase-locking of microwave spin torque nano-oscillators, Nature **437,** 389 (2005).

[22] F. B. Mancoff, N. D. Rizzo, B. N. Engel, and S. Tehrani, Phase-locking in double-point-contact spin-transfer devices, Nature **437,** 393 (2005).

[23] S. M. Rezende, F. M. de Aguiar, R. L. Rodríguez-Suárez, and A. Azevedo, Mode Locking of Spin Waves Excited by Direct Currents in Microwave Nano-Oscillators, Phys. Rev. Lett. **98,** 087202 (2007).

[24] A. Ruotolo, V. Cros, B. Georges, A. Dussaux, J. Grollier, C. Deranlot, R. Guillemet, K. Bouzehouane, S. Fusil, and A. Fert, Phase-locking of magnetic vortices mediated by antivortices, Nat. Nanotechnol. **4,** 528 (2009).

[25] N. Locatelli, A. Hamadeh, F. Abreu Araujo, A. D. Belanovsky, P. N. Skirdkov, R. Lebrun, V. V. Naletov, K. A. Zvezdin, M. Muñoz, J. Grollier, O. Klein, V. Cros, and G. de Loubens, Efficient synchronization of dipolarly coupled vortex-based spin transfer nano-oscillators, Sci. Rep. **5,** 17039 (2015).

[26] M. Zahedinejad, A. A. Awad, S. Muralidhar, R. Khymyn, H. Fulara, H. Mazraati, M. Dvornik, and J. Åkerman, Two-dimensional mutually synchronized spin hall nano-oscillator arrays for neuromorphic computing, Nat. Nanotechnol. **15,** 47 (2020).

[27] J.-V. Kim, V. Tiberkevich, and A. N. Slavin, Generation Linewidth of an Auto-Oscillator with a Nonlinear Frequency Shift: Spin-Torque Nano-Oscillator, Phys. Rev. Lett. **100,** 017207 (2008).

[28] W. H. Rippard, M. R. Pufall, S. Kaka, T. J. Silva, S. E. Russek, and J. A. Katine, Injection Locking and Phase Control of Spin Transfer Nano-Oscillators, Phys. Rev. Lett. **95,** 067203 (2005).

[29] B. Georges, J. Grollier, M. Darques, V. Cros, C. Deranlot, B. Marcilhac, G. Faini, and A. Fert, Coupling Efficiency for Phase Locking of a Spin Transfer Nano-Oscillator to a Microwave Current, Phys. Rev. Lett. **101,** 017201 (2008).

[30] V. E. Demidov, H. Ulrichs, S. V. Gurevich, S. O. Demokritov, V. S. Tiberkevich, A. N. Slavin, A. Zholud, and S. Urazhdin, Synchronization of spin hall nano-oscillators to external microwave signals, Nat. Commun. **5,** 3179 (2014).

[31] S. Tsunegi, E. Grimaldi, R. Lebrun, H. Kubota, A. S. Jenkins, K. Yakushiji, A. Fukushima, P. Bortolotti, J. Grollier, S. Yuasa, and V. Cros, Self-injection locking of a vortex spin

torque oscillator by delayed feedback, Sci. Rep. **6,** 26849 (2016).

[32] S. Tamaru, H. Kubota, K. Yakushiji, S. Yuasa, and A. Fukushima, Extremely coherent microwave emission from spin torque oscillator stabilized by phase locked loop, Sci. Rep. **5,** 18134 (2015).

[33] Ö. O. Soykal, and M. E. Flatté, Strong Field Interactions between a Nanomagnet and a Photonic Cavity, Phys. Rev. Lett. **104,** 077202 (2010).

[34] H. Huebl, C. W. Zollitsch, J. Lotze, F. Hocke, M. Greifenstein, A. Marx, R. Gross, and S. T. B. Goennenwein, High Cooperativity in Coupled Microwave Resonator Ferrimagnetic Insulator Hybrids, Phys. Rev. Lett. **111,** 127003 (2013).

[35] X. Zhang, C.-L. Zou, L. Jiang, and H. X. Tang, Strongly Coupled Magnons and Cavity Microwave Photons, Phys. Rev. Lett. **113,** 156401 (2014).

[36] Y. Tabuchi, S. Ishino, T. Ishikawa, R. Yamazaki, K. Usami, and Y. Nakamura, Hybridizing Ferromagnetic Magnons and Microwave Photons in the Quantum Limit, Phys. Rev. Lett. **113,** 083603 (2014).

[37] L. Bai, M. Harder, Y. P. Chen, X. Fan, J. Q. Xiao, and C.-M. Hu, Spin Pumping in Electrodynamically Coupled Magnon-Photon Systems, Phys. Rev. Lett. **114,** 227201 (2015).

[38] Y. Tabuchi, S. Ishino, A. Noguchi, T. Ishikawa, R. Yamazaki, K. Usami, and Y. Nakamura, Coherent coupling between a ferromagnetic magnon and a superconducting qubit, Science **349,** 405 (2015).

[39] Y. Cao, P. Yan, H. Huebl, S. T. B. Goennenwein, and G. E. W. Bauer, Exchange magnon-polaritons in microwave cavities, Phys. Rev. B **91,** 094423 (2015).

[40] W. Yu, J. Wang, H. Y. Yuan, and J. Xiao, Prediction of Attractive Level Crossing via a Dissipative Mode, Phys. Rev. Lett. **123,** 227201 (2019).

[41] Y. Li, T. Polakovic, Y.-L. Wang, J. Xu, S. Lendinez, Z. Zhang, J. Ding, T. Khaire, H. Saglam, R. Divan, J. Pearson, W.-K. Kwok, Z. Xiao, V. Novosad, A. Hoffmann, and W. Zhang, Strong Coupling between Magnons and Microwave Photons in On-Chip Ferromagnet-Superconductor Thin-Film Devices, Phys. Rev. Lett. **123,** 107701 (2019).

[42] J. T. Hou and L. Liu, Strong Coupling between Microwave Photons and Nanomagnet Magnons, Phys. Rev. Lett. **123,** 107702 (2019).

[43] W. E. Lamb, Theory of an optical maser, Phys. Rev. **134,** A1429 (1964).

[44] M. Borenstein and W. E. Lamb, Classical laser, Phys. Rev. A **5,** 1298 (1972).

[45] J. D. Breeze, E. Salvadori, J. Sathian, N. M. Alford, and C. W. M. Kay, Continuous-wave room-temperature diamond maser, Nature **555,** 493 (2018).

[46] A. Vansteenkiste, J. Leliaert, M. Dvornik, M. Helsen, F. Garcia-Sanchez, and B. Van Waeyenberge, The design and verification of MuMax3, AIP Adv. **4,** 107133 (2014).

[47] For modified MUMAX3 codes with spin-resonator coupling, see: https://github.com/jthou-spin/MuMax3-spinresonator.git.

[48] B. Divinskiy, S. Urazhdin, S. O. Demokritov, and V. E. Demidov, Controlled nonlinear magnetic damping in spin-hall nano-devices, Nat. Commun. **10,** 5211 (2019).

[49] M. Göppl, A. Fragner, M. Baur, R. Bianchetti, S. Filipp, J. M. Fink, P. J. Leek, G. Puebla, L. Steffen, and A. Wallraff, Coplanar waveguide resonators for circuit quantum electrodynamics, J. Appl. Phys. **104,** 113904 (2008).

[50] A. Slavin and V. Tiberkevich, Excitation of spin waves by spin-polarized current in magnetic nano-structures, IEEE Trans. Magn. **44,** 1916 (2008).

[51] H. Hong, H. Park, and M. Y. Choi, Collective synchronization in spatially extended systems of coupled oscillators with random frequencies, Phys. Rev. E **72,** 036217 (2005).

[52] V. Flovik, F. Macià, and E. Wahlström, Describing synchronization and topological excitations in arrays of magnetic spin torque oscillators through the Kuramoto model, Sci. Rep. **6,** 32528 (2016).

[53] E. Ott and T. M. Antonsen, Low dimensional behavior of large systems of globally coupled oscillators, Chaos **18,** 037113 (2008).

[54] M. M. Abdulrehem and E. Ott, Low dimensional description of pedestrian-induced oscillation of the millennium bridge, Chaos **19,** 013129 (2009).

[55] M. W. Keller, M. R. Pufall, W. H. Rippard, and T. J. Silva, Nonwhite frequency noise in spin torque oscillators and its effect on spectral linewidth, Phys. Rev. B **82,** 054416 (2010).

[56] J. C. Bardin, D. H. Slichter, and D. J. Reilly, Microwaves in quantum computing, IEEE J. Microw. **1,** 403 (2021).

[57] F. A. Hopf, P. Meystre, M. O. Scully, and W. H. Louisell, Classical theory of a free-electron laser, Opt. Commun. **18,** 413 (1976).

[58] W. B. Colson, One-body electron dynamics in a free electron laser, Phys. Lett. A **64,** 190 (1977).

[59] M. C. Cassidy, A. Bruno, S. Rubbert, M. Irfan, J. Kammhuber, R. N. Schouten, A. R. Akhmerov, and L. P. Kouwenhoven, Demonstration of an ac josephson junction laser, Science **355,** 939 (2017).

[60] S. H. Simon and N. R. Cooper, Theory of the Josephson Junction Laser, Phys. Rev. Lett. **121,** 027004 (2018).

[61] S. H. Strogatz, D. M. Abrams, A. McRobie, B. Eckhardt, and E. Ott, Crowd synchrony on the millennium bridge, Nature **438,** 43 (2005).